Arabian Journal of Geosciences (2023) 16:683
https://doi.org/10.1007/s12517-023-11737-y

ORIGINAL PAPER

Failure mechanism analysis and mass movement assessment of a post-earthquake high slope

Chong-xun Wang[1] · Jia-wen Zhou[2] · Chang-bing Zhang[1] · Yu-xiang Hu[2] · Hao Chen[3] · Hai-bo Li[1]

Received: 18 April 2023 / Accepted: 19 October 2023 / Published online: 30 November 2023
© Saudi Society for Geosciences and Springer Nature Switzerland AG 2023

Abstract

Landslides induced by rainfall pose a notable threat to post-earthquake reconstruction in mountainous areas. Taking Qingliu landslide as an example, this paper reveals the potential failure mechanism and range of the landslide mass through field investigation and monitoring data, and further uses the improved computational fluid dynamics method to simulate and predict the disaster range after landslide destabilization. The results show that the landslide was initially deformed and cracked under the influence of strong earthquakes and formed seepage channels for water infiltration. The circulation of surface recharge of groundwater in rainy season and long-distance recharge of groundwater from melting ice and snow in winter season leads to the continuous softening and reduction of sliding resistance in the sliding zone. Under the action of this change chain, the cracks along the back edge and boundary of the landslide continue to develop and expand and finally will lead to landslide collapse failure. The equivalent fluid method can better simulate the movement process and accumulation process of landslide, since the Qingliu landslide is a soil landslide with fluid characteristics in the process of landslide movement. The results indicate that the maximum speed of the mass flow could reach 49 m/s, which could destroy the infrastructures along the sliding path, besides, both of the two landslides could bury Xiameng town below and block the Mengtun River to form a landslide-dammed lake. The research results could provide a reference for further comprehensive treatment of landslides and the formulation of emergency plans.

Keywords Earthquake damaged slope · Failure mechanism · Equivalent fluid simulation method · Disaster-causing impact

Introduction

Landslides are natural hazards worldwide that pose a serious threat to the population in various areas (Petley 2012). In recent years, the frequency and scale of landslides have increased due to several strong earthquakes and extreme weather events. Fractures caused by strong earthquakes can increase the frequency of landslides (Fan et al. 2019; Li et al. 2019a), and a substantial number of landslides are triggered by rainfall after earthquakes. Over 56,000 landslides were activated by the Wenchuan earthquake (Dai et al. 2011), which resulted in the destruction and burial of villages, river blockage (Huang et al. 2011), and heavy casualties (Yin et al. 2009). There have been several large landslides over the past few years in Southwest China. In the afternoon of 28 June 2010, a catastrophic landslide occurred in Guanling County, Guizhou Province; 99 people were killed, and two villages were buried (Kang et al. 2017). On 24 June 2017, under the influence of heavy rainfall, a massive rock avalanche destroyed the village of Xinmo in Maoxian County, Sichuan Province, causing 10 deaths with over 70 people missing (Fan et al. 2017). On 11 October 2018, the Baige landslide suddenly occurred in Baiyu County, Tibet, Southwest China. The sliding mass crashed into the Jinsha River and formed a landslide dam with an average height of 80 m.

Additionally, the uncertainty in the evaluation of the impacts of climate change on landslides and the stability of natural and engineered slopes has increased in response to climate change and human activities (Gariano and Guzzetti

Responsible Editor: Zeynal Abiddin Erguler

✉ Hai-bo Li
hbli@scu.edu.cn

[1] College of Water Resource and Hydropower, Sichuan University, Chengdu 610065, China

[2] State Key Laboratory of Hydraulics and Mountain River Engineering, Sichuan University, Chengdu 610065, China

[3] Sichuan Water Resources and Hydroelectric Investigation and Design Institute, Chengdu 610072, China

2016). Thus, a large number of researchers and experts have studied landslides through various technical means and analysis methods in recent years. Nevertheless, the disaster mechanism remains unclear because of climate, hydrology, geology, and human activities. Furthermore, the development processes vary due to the material composition and structure of landslide formation.

Rainfall and earthquakes are crucial factors that cause landslides; for example, the Shuicheng landslide (Li et al. 2020) and Tonghua landslide (Wang et al. 2019) were mainly triggered by heavy rainfall, while the Xinmo landslide (Fan et al. 2017) was the result of the interaction among multiple factors. In addition, the movement process of landslides is complicated and changes with various factors (Fan et al. 2017; Hu et al. 2019; Kang et al. 2017; Li et al. 2019b; Wang et al. 2019). Landslide movement simulation is a crucial strategy to analyze and predict the potential disaster-influenced areas. Numerical simulation is utilized to study the process of submarine landslide with the aim of identifying the whole failure process, besides providing forecasting and early warning of the disasters (Shan et al. 2022). The results obtained via discontinuous deformation analysis (DDA) suitably agreed with field observation data (Do and Wu 2020; Zhang et al. 2013). Wei et al. (2019) utilized the particle flow code (PFC) to investigate the kinetic characteristics of the Mabian landslide, and the simulation results were consistent with the actual landslide characteristics, which could provide a theoretical reference for quantitative risk evaluation of landslides in the area and disaster prevention and mitigation. Zhuang et al. (2020) used the DAN3D method to investigate the Yigong rock slide-debris avalanche; the DAN3D simulation results suitably agreed with the actual event in terms of the deposit distribution, landslide volume, and run-out distance. Liu et al. (2021a, b) successfully predicted the propagation of debris flows and structural failure by incorporating complicated fluid-particle-structure interactions (FPSIs) using a coupled smoothed particle hydrodynamics (SPH), discrete element method (DEM), and finite element method (FEM) approach. Liu et al. (2021a, b) revealed the destruction process and dynamics characteristics of the XGJ rockslide, and the simulated movement path and depositional area agreed with field investigation data, which could provide a technical basis for comprehensive risk assessment and disaster reduction in fractured mountains. Wu et al. (2023) set up three kinds of rapid prediction model of landslide dam through the method of smoothed particle hydrodynamics (SPH) providing a reference for the landslide dam formation. The models proposed are shown to be effective via comparisons with the actual condition and simulation results. Thus, it is of vital importance to evaluate stability and study the potential disaster-causing mechanism for prevention and mitigation purposes.

This paper investigated an earthquake-damaged slope, namely, the Qingliu village landslide, which developed under the influence of the Wenchuan earthquake and experienced deformation under the condition of rainfall and groundwater. Two unstable landslides evolved in the study area, namely, the H01 landslide and the H02 landslide. The H01 landslide occurred on December 4, 2020, and a portion of the sliding mass rushed into the Mengtun River at the toe of the slope, thereby blocking the river and forming a landslide dammed lake. Fortunately, no casualties ensued. Affected by earthquakes and concentrated rainfall, however, the slope could still possibly slide again and generate potential hazards, which could pose a notable threat to the safety of life and property and cause serious damage to the ecological environment and infrastructure. Through theoretical analysis and numerical simulation, this paper studied the stability and disaster-causing effect of the earthquake-damaged slope in Qingliu village, Li County, and provided a reference for emergency treatment and disaster loss reduction.

Background

The Wenchuan earthquake was the strongest and most destructive earthquake that impacted China over the past century, killing 69227 people and triggering massive landslides (Dai et al. 2011), for instance, the Daguangbao landslide (Huang et al. 2011), Wangjiayan landslide, Jingjiashan landslide (Zhang et al. 2014), and other directly influenced landslide disasters. The intense shocks during this earthquake caused numerous unstable slopes, and loose deposited material accumulated (Cui et al. 2009), indirectly resulting in seismic damage to many slopes under the single or combined effects of rainfall, earthquakes, and other factors, such as the Xishanpo gully debris flow (Tang et al. 2009), Tonghua landslide (Wang et al. 2019), and Gaojiagou Ravine debris flow (Fan et al. 2018).

The Qingliu village landslide is situated on the left bank of the Zagunao River in the town of Xiameng, Li County (Fig. 1b), a typical landslide triggered by the Wenchuan earthquake, approximately 67 km away from the Wenchuan earthquake epicenter. The peak acceleration of this earthquake was 0.15 g (Fig. 1a), the characteristic period of the ground motion response spectrum was 0.40 s, and the basic seismic intensity reached degrees VII~VIII. Li County is situated in Sichuan Province in Southwest China (Fig. 1c), in the middle of the Longmenshan fault zone, which is one of the 29 quake-affected counties of the Wenchuan earthquake. High mid-mountain houses were all damaged during the earthquake; moreover, affected by notable seismic activity, the slope was loosened under earthquake amplification, and relaxation failure of the slope could be observed.

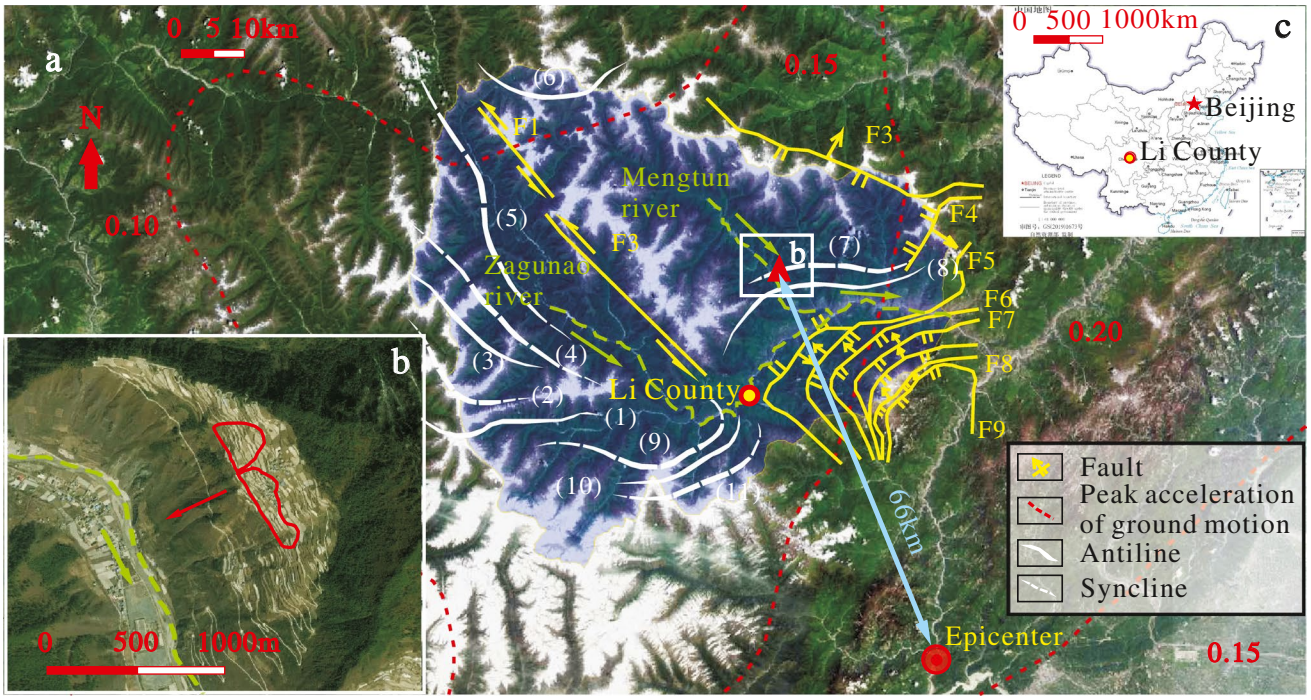

Fig. 1 Location of the Qingliu village landslide and geological structure map of Li County: **a** location of the Qingliu village landslide and **b** top view of the landslide area and **c** map of China

After heavy rain in June 2020, collapse deformation occurred in the strong deformation I area of H01 (Fig. 2c) and strong deformation of H02 (Fig. 2d), and loose material accumulated in the landslide source area and lower gully. The landslide mass rapidly moved downward along the lower gully and destroyed houses along the way, with a volume of 6.1×10^4 m^3. Part of the landslide accumulated in the source area, and the volume reached approximately 0.5×10^4 m^3. A large portion of the landslide rushed into the Mengtun River with a volume of approximately 2.6×10^4 m^3, blocking the river and forming a landslide-dammed lake. The maximum height of the weir was approximately 6 m, the length along the river was approximately 100 m, and the width across the river was approximately 80 m (Fig. 3b).

The study area is situated in the transition zone between the southeastern Qinghai-Tibet Plateau and the Sichuan Basin, with mountains and a range of hills stretching across Li County. The summit exhibits an elevation of more than 4000 m above sea level. The relative height difference in the valley ranges from 800 to 1200 m, which belongs to tectonic denudation and alpine landforms. The landslide developed on the terrace of the Mengtun River (Fig. 2a), whose strike direction is 241°; moreover, the height difference from the river is approximately 500 m, and the terrain is gentler in the upper part with a slope degree between 25° and 35°, while the terrain is steeper in the lower part with a slope degree between 35° and 45°, and the terrain shows "U" type (Fig. 2b). After several diastrophic processes within the territory, the study area was primarily influenced by the S-type structure of Xuecheng and the compound synclinal structure of Xiameng. As shown in Fig. 1a, the rock mass was fractured owing to the transection of the mountains by the compound synclinal structure of Xiameng. The main river within Li County, i.e., the Zagunao River, flows through the landscape from northwest to southeast. The Mengtun River is the largest tributary in the Zagunao River basin, with an average aspect of 56.35‰.

In the study area, the primary surface formations include Quaternary Holocene colluvial gravel soil (Q_4^{col+dl}), Upper Pleistocene glacial accumulations of crushed silty clay layers Q_4^{fgl}, and bedrock comprising Triassic–Jurassic Upper Juwa (T_3zh) Formation phyllite intercalated sand and slate layers (Fig. 3a). Slope diluvial loess-like gravel silty clay (Q_4^{dl+pl}) consisted large of loess-like gravel silty clay is mainly distributed at the steep slopes and gentle slopes occurring above of the landslide area. The rock layers form an upright steep slope with a height of approximately 1.5 ~ 3 m on the surface, and vertical fractures are mostly developed, often resulting in small-scale slumps (Fig. 4b).

Groundwater is enriched in the study area and mainly consists of bedrock fissure water, which is supplied by atmospheric precipitation, mountain snowmelt water, agricultural irrigation, and surface water. Controlled by the terrain conditions and solid structure, the groundwater exhibits

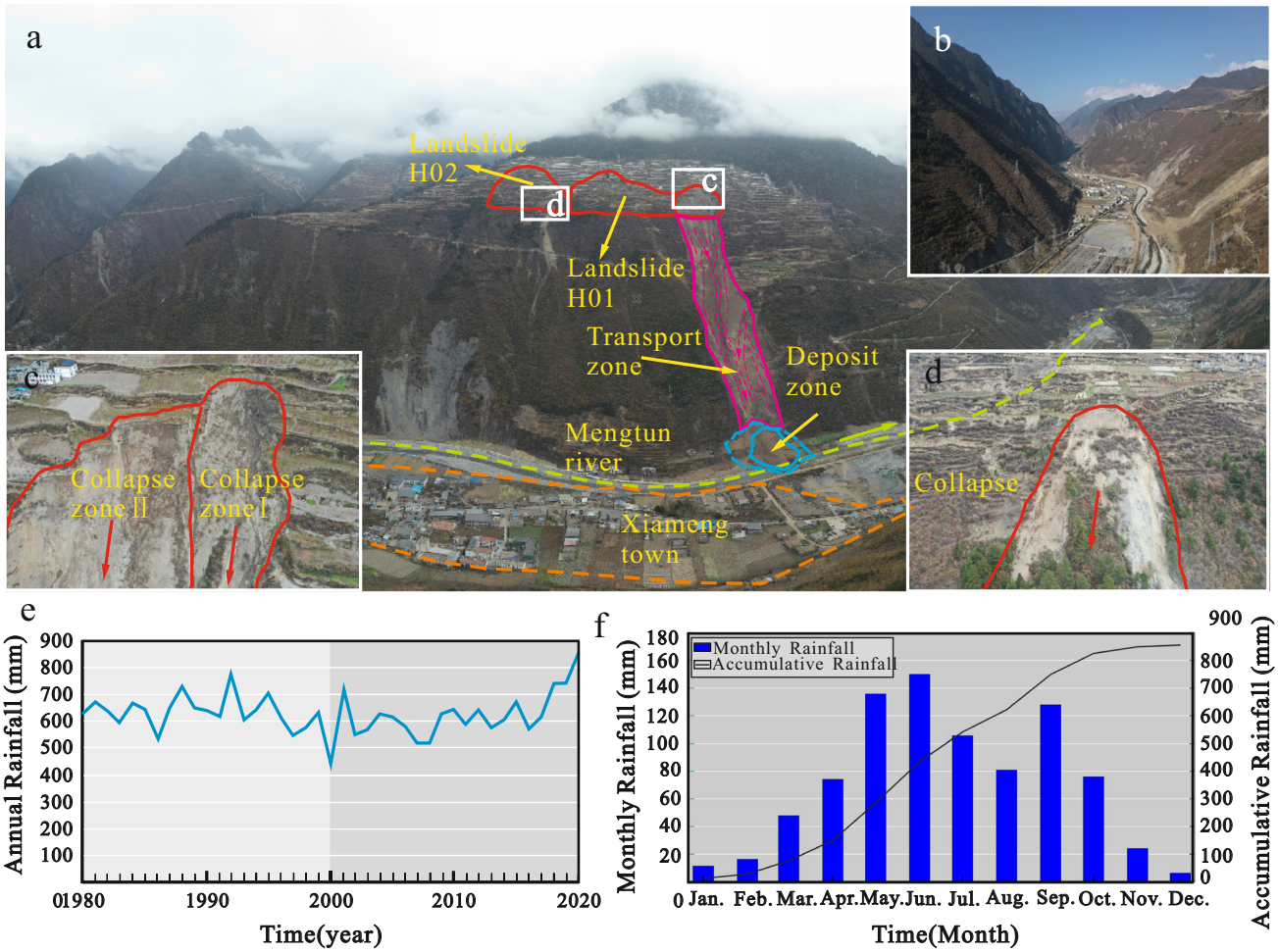

Fig. 2 Landscape and rainfall in the study area (Li et al. 2023): **a** general view of the Qingliu village landslide, **b** the terrain in the landslide area indicates a U-type canyon, **c** strong deformation area of the H01 landslide, **d** strong deformation area of the H02 landslide, **e** annual rainfall in the study area over the last 40 years, and **f** monthly and accumulative rainfall levels in 2020

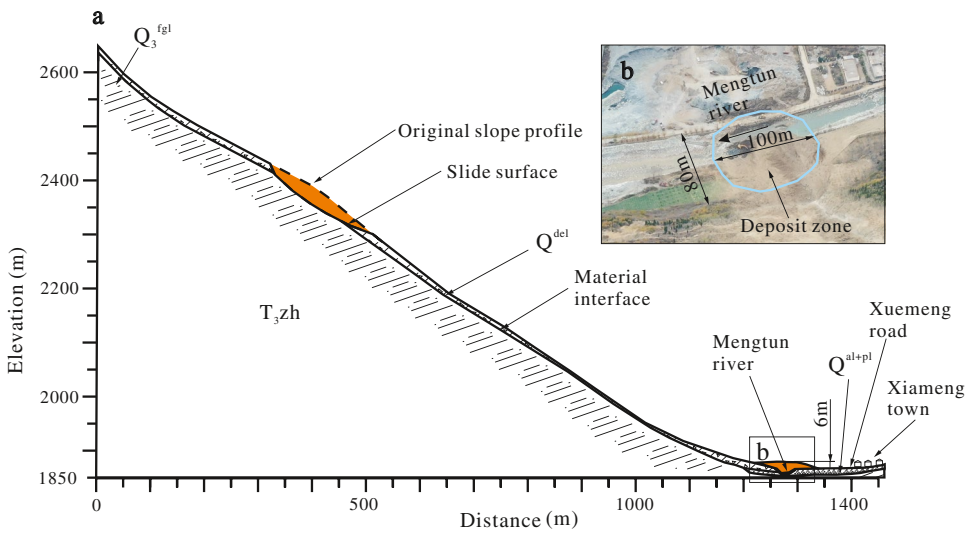

Fig. 3 Geological section map of the Qingliu village landslide

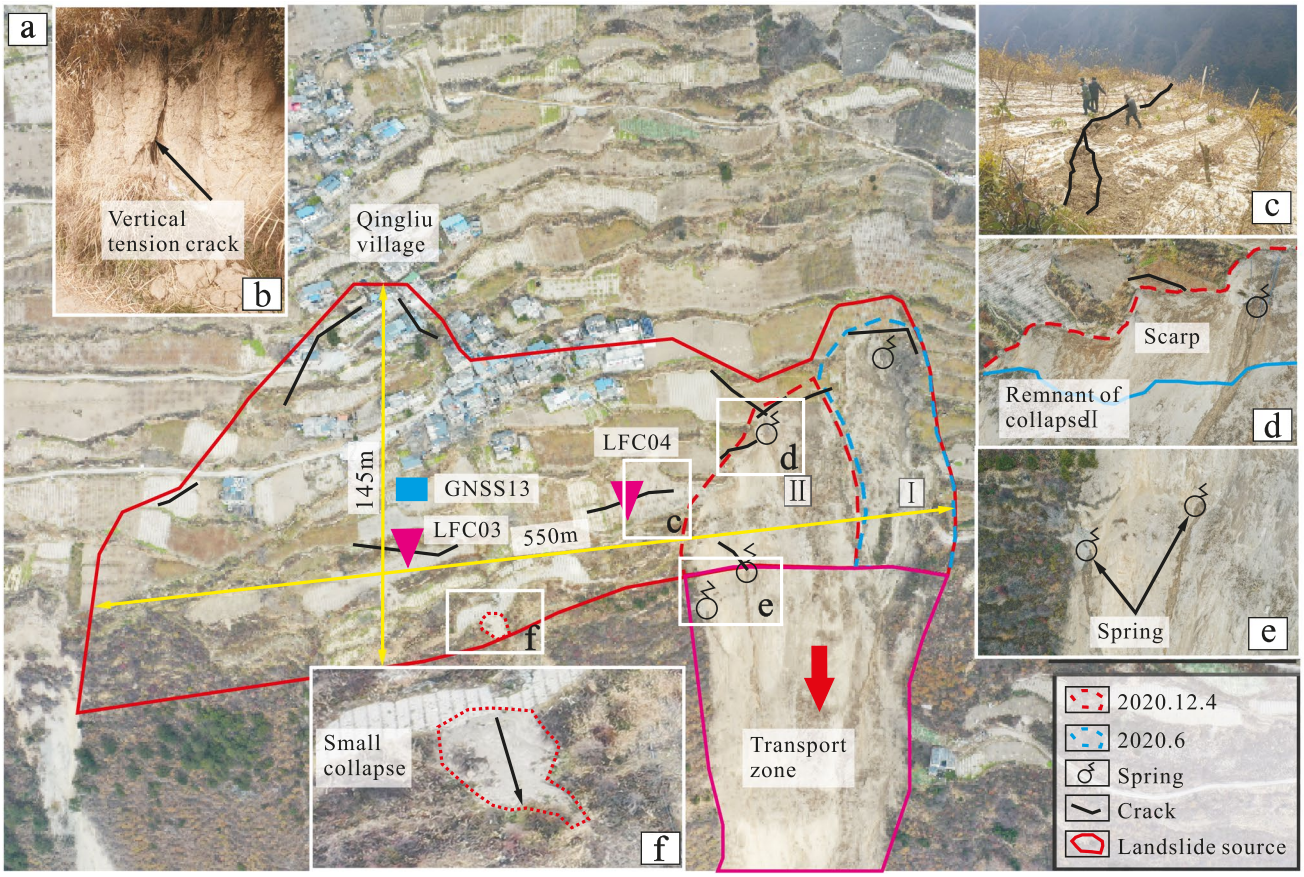

Fig. 4 Landscape of the H01 landslide: **a** deformation overview of the H01 landslide, **b** vertical crack in the surface accumulation body, **c** crack in the landslide, **d** remnant of collapse II, **e** exposed springs at the bottom of the landslide, and **f** small collapse in the landslide area

the characteristics of an uneven distribution and a varying groundwater level. Furthermore, rainfall is unevenly distributed throughout the year in Li County and is characterized by a bimodal distribution, which suggests that there are two rainfall peaks. The main rainfall peak occurs in June, and rainfall from May to June accounts for 33.4% of the annual rainfall (Li et al. 2023). Moreover, the second rainfall peak occurs in September, and the precipitation from March to October accounts for 93.24% of the annual precipitation.

Failure mechanism and stability analysis of landslides

Scale and characteristics of landslide deformation

The landslide can be divided into two landslides by multiple fractures, namely, the H01 landslide and H02 landslide, as shown in Fig. 2a, both of which are retrogressive landslides. The landslide first experienced deformation after the Wenchuan earthquake on May 12, 2008, and deformation occurred after heavy rain during the rainy season and after groundwater recharge with snowmelt water in winter. The landslide first formed after effect of the "Wenchuan earthquake" and then went through a long period of deformation which along with cracks development and small collapses. Deformation of the landslide presents different in time and area; in general, they are related to the heavy rain. Finally the landslide revived under the influence of continuous rainfall in 2020.

The H01 landslide exhibits a long lateral extension and appears rectangular overall. The height of the front edge is approximately 2300 m, and the height of the back edge is approximately 2410 m. The length of the landslide ranges from 110 to approximately 145 m, the width is approximately 550 m (Fig. 4a), the maximum height difference between the front and back edges is approximately 110 m, the average thickness of the sliding body is approximately 17 m, and the total volume reaches approximately 1.1×10^6 m^3. The trailing edge of the landslide is bounded by tensile fractures (Fig. c), the leading edge is bounded by bedrock outcrops or shallow buried areas, and the surface of the landslide is bounded by gullies on both sides. The slope of the landslide is approximately 40° in the lower part and 25 ~ 35° in the middle and upper parts, while the lower part contains a free face.

Cracks emerged along the back edge of the landslide during the earthquake, and the strength of the landslide was reduced by the notable earthquake disturbance. Thereafter, under the action of rainfall and gravity, a large number of tensile cracks emerged, which were widely distributed along the back edge of the landslide, with obvious openings and drop ridges, and the strike was almost perpendicular to the sliding direction of the landslide. Additionally, there are vertical cracks in the surface accumulation body within the landslide area (Fig. 4b), several small collapses occur in the landslide area (Fig. 4f), and there is a lack of stability. Springs are exposed below and on the side of the landslide (Fig. 4d, 4e, respectively). The trailing edge of the H01 landslide is steep as a result of slump deformation (Fig. 4d). The strong deformation II area of H01 exhibited increasing deformation under long-term unloading since the rainy season that year. Moreover, tension cracks were created along the trailing edge, and deformation continued under the action of gravity and groundwater in October. Before the collapse on December 4, tensile fractures with apparent drop ridges along the trailing edge reached 60 ~ 100 cm and the openings reached approximately 20 ~ 30 cm, followed by collapse deformation.

The H02 landslide exhibits the shape of an armchair at the rear edge, the leading edge elevation is approximately 2290 m, the trailing edge elevation is approximately 2480 m, and the maximum height difference between the front and back edges is approximately 190 m. The length of the landslide is approximately 270 m, the width is approximately 200 m, the average thickness of the landslide body is approximately 20 m, the total volume is approximately 8×10^5 m^3, and the terrain slope is approximately 35°.

The H02 landslide is characterized by numerous tension cracks with distinct drop ridges (Fig. 5a). The landslide further moves under the drag force of the front sliding body, thus forming extensive tension cracks, which are mainly distributed across the rear slope (Fig. 5c) and along the road (Fig. 5b). A spring is exposed on the right side of the strong deformation area (Fig. 5d). The thickness of the slope accumulation is large, and the stability is poor, which results from several collapses within the area (Fig. 5d). The strong deformation area of the landslide was preceded by a landslide on September 14, 2020, and the soil along the leading edge of the strongly deformed area collapsed. A mass accumulated on the lower slope and road, resulting in road blockage (Fig. 5g). The trailing edge of the strong deformation zone extended downward up to 2 m (Fig. 5f), while the height of the rear reached up to 1.5 m on average (Fig. 5e).

Tensile fractures were generated on the rear slope attributable to retrogressive action (Fig. 4c), and multiple fractures were developed in the middle and rear parts of the affected slope under the action of gravity and groundwater (Fig. 5c–f), whose strike was almost vertical to the sliding direction of the landslide. Along the back edge of the H02 landslide in the strong deformation zone, the drop ridges reached 5 m, and boundary cracks were connected as a whole, occurring in a state of an impending slide.

In regard to landslide deformation monitoring, monitoring instruments were installed on the surface and cracks of the slope. Over the past 8 months, surface deformation monitoring data of the GNSS06 monitoring site at the rear of the H02 landslide strong deformation area showed that the average daily displacement deformation at this site from May to August 2021 was 5.8, 12.8, 8.4, 6.4, and 4 mm/day, and the average daily displacement at GNSS01 and GNSS02 from May to September 2021 reached 8.8, 15.6, 11.3, 10.4, and 4.3 mm/day and 6.5, 11.3, 8.4, 6.6, and 2.6 mm/day, respectively. The data of LFC02, a monitoring point in a rear crack of the H02 landslide, showed that the cumulative displacement from May to July exhibited an increasing trend, and the average daily displacement reached 42.3 mm/day from August 9 to 15. As shown in Fig. 2e, f, the annual rainfall in the study area showed an increasing trend over the last two decades, and in 2020, it reached a new peak. Figures 2f and 6a show that the rainfall and accumulative deformation, respectively, were consistent, which suggests that rainfall may be responsible for the continuous deformation. The average daily cumulative displacement at LFC01, a monitoring point in the rear crack of the H02 landslide, was 5.7, 9.2, and 18.1 mm/day from May to July, and the displacement was positively correlated with rainfall. The displacement in the H02 landslide strong deformation area was larger than that along the back edge (Fig. 6). Large landslide deformation occurred on October 15 and 24, 2021 (Fig. 6a and 6b, respectively). The H02 landslide developed multiple extensional fractures with continuous expansion of the deformation scale and occurs at the creep deformation stage, which may lead to overall retrogressive instability.

According to the overall monitoring data, the deformation of the H01 landslide was small. The deformation at the LFC03 monitoring point in a crack remained stable after it suddenly changed from 0.5 mm to 938.2 mm on August 4, 2021, and the crack at LFC04 GNSS13 basically remained stable. Nonetheless, because H01 developed multiple fractures, part of the slumped body accumulated in the slide source area, and several small-scale collapses occurred in the landslide area. Moreover, the landslide still has the possibility of collapse.

Failure mechanism of landslides

Both of the landslides are shallow to medium retrogressive landslides, and between them, the H02 landslide is a typical example. This landslide exhibits notable traction characteristics from the perspective of the previous landslide. The lower sliding body first slid, and the upper soil lost its support, resulting in the extension of the sliding upward slope in the process (Zhou et al. 2014).

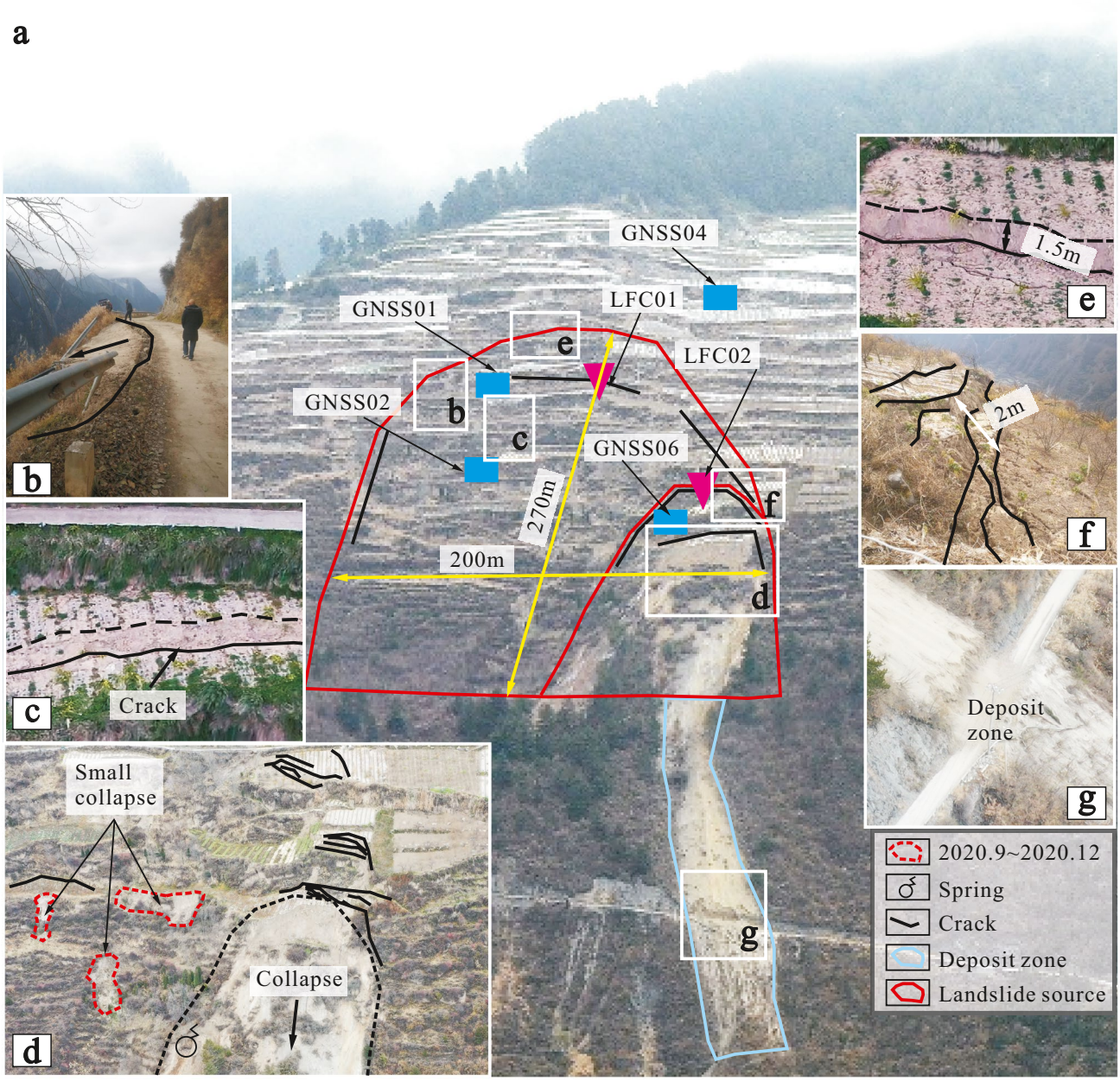

Fig. 5 Landscape of the H02 landslide: **a** deformation overview of the H02 landslide, **b** road deformation, **c** drop ridge at the rear of the H02 landslide, **d** cracks and collapses around the strong deformation zone, **e** crack in the, **f** deformation along the back edge of the strong deformation area, and **g** slump accumulated on the lower road

The stability of a landslide is influenced by its material composition, structure, and environment, among which rainfall, earthquakes, and human activities are the most notable environmental factors inducing landslide occurrence. Frequent and intensive human activities, including farming, infrastructure development, and house construction, lead to a great change in the landslide surface morphology, which complicates the failure mechanism of landslides and accelerates the process of landslide evolution to a certain extent. After the "Wenchuan earthquake," cracks occurred on the top of the slope, besides, springs, and underground water increased apparently. It is speculated that the earthquake action contributes to the cracks opening of the slope increased. The seismic amplification makes it even worse to the mountainous area, for example, this study area. The connectivity of the cracks is promoted making for the groundwater activity; meanwhile, the slope is tend to be loosen.

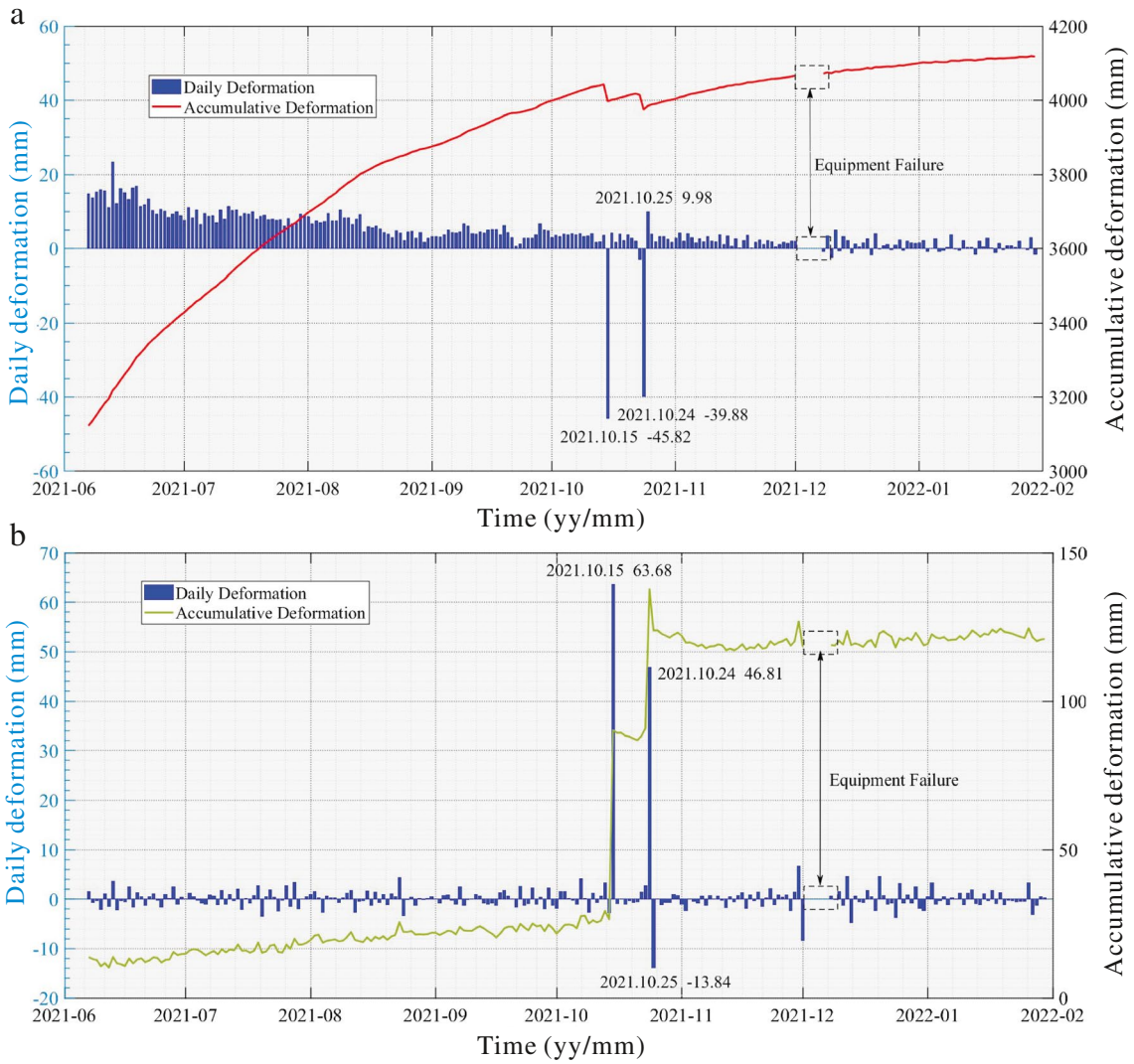

Fig. 6 Daily and accumulative deformation data collected from June 7, 2021, to January 30, 2022, with a lack of data from December 2, 2021, to December 6, 2021, due to equipment failure: **a** displacement monitoring data of GNSS06 and **b** displacement monitoring data of GNSS04

The primary landslide component is silty clay, which contains a high clay content and easily softens under the action of water. Landslides are prone to sliding because of their high locality and free face. With increasing population and economic development, slope excavation increasingly occurs in construction and reclaimed land, resulting in slope cutting, which destroys the original stress balance of the slope body and affects local soil stability.

The landslide initially experienced deformation under the influence of strong earthquakes (Fig. 7a, b); thereafter, slope damage occurred during both the rainy and winter seasons, with different failure mechanisms, and water is the crucial factor in the failure process. Village road instability from 2013 to 2015 and landslide instability and deformation of the H01 landslide in June and September 2020 were prompted by heavy rainfall, while tension cracks and collapse deformation of the H01 and H02 landslides were mainly triggered by groundwater. The effects of groundwater on rock and soil can mainly be divided into physical and mechanical effects.

There is a large amount of concentrated rainfall during the rainy season in Li County, and the characteristics of landslide damage are as follows: concentrated rainfall, surface recharge of groundwater, softening and a reduction in the sliding resistance in the sliding zone, tensile fracturing of the sliding body, and collapse failure (Fig. 7). Rainwater infiltration increases the water content in the slope and the dead weight of the sliding body, resulting in saturated seepage. Under the action of saturated seepage, the landslide constantly produces tensile cracks, which reduces its stability. The infiltration of groundwater in the sliding zone produces physical and chemical effects, which reduce the friction and cementation among soil particles, the shear strength in the sliding zone gradually decreases, and shear failure occurs in the soil of the landslide, eventually leading to overall or partial collapse (Fig. 7c, d).

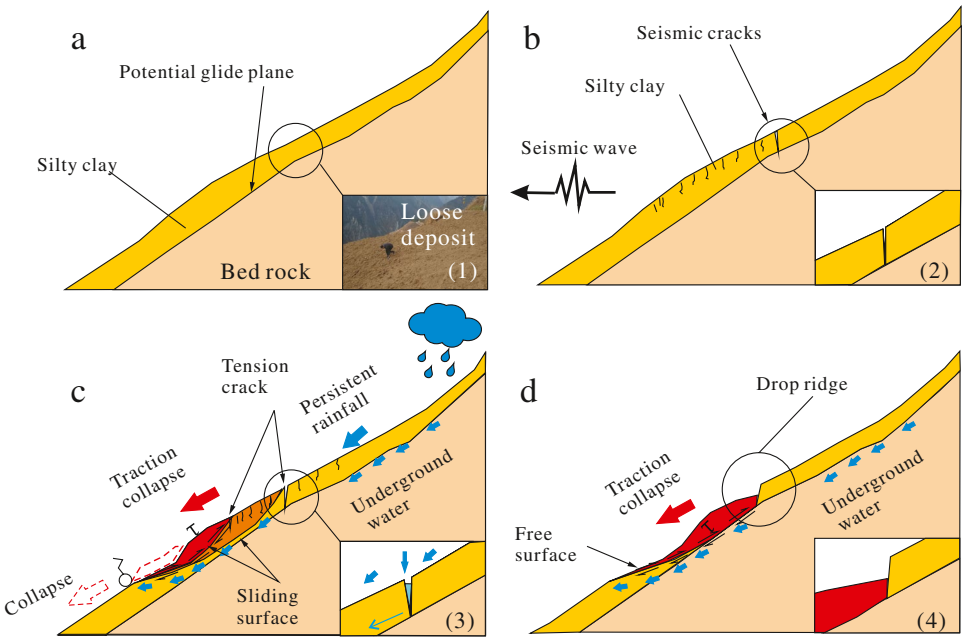

Fig. 7 Failure mechanism of the retrogressive landslides in Qingliu village: **a** loose material is deposited on the slope; **b** cracks are induced after the earthquake; **c** collapses occur under the combined action of rainfall, gravity, and underground water; and **d** drop ridges are formed and traction collapse occurs

The winter is dry with little rain, and landslide deformation is mainly affected by groundwater. The mountain in the northeast of the landslide area is covered with snow in winter. The air temperature rises at noon, and alpine snow melts, which continuously supplies groundwater in the landslide area along underground seepage channels. The characteristics of landslide failure in winter are as follows: melting of alpine snow, remote recharge of groundwater, softening in the slip zone, and tensile cracking of the slip body and collapse failure. Snowmelt water extensively replenishes groundwater, and landslide deformation continues to increase based on the accumulated deformation due to rainfall and gravity. The pore water pressure between the soil particles increases, and the dynamic water pressure produces tangential thrust in the soil, which increases the sliding force of the landslide and reduces the shear strength of the sliding surface. Groundwater in the landslide area exerts a traction effect on the upper part of the landslide, which causes tensile fracture along the back edge of the landslide. Under the action of this change chain, the cracks along the back edge and boundary of the landslide continue to develop and expand, finally leading to landslide collapse failure.

Numerical simulation of the landslide dynamic evolution process

According to the above analysis, the sliding area of the H02 landslide occurs at the stage of continuous deformation, and its safety should be further studied. There is a possibility of further sliding in the case of subsequent rainfall, groundwater, and earthquakes. In addition, there are infrastructures and residential areas downstream of the slope that are likely to be affected by the landslide. To study the movement process and ascertain the potential affected area, the whole process of landslide start-up and sliding accumulation was simulated to analyze the potential disaster effect of landslides. Although there is no large-scale displacement between the strong deformation zones of the H01 landslide and the H02 landslide, it was included in the calculation scope for disaster prevention and mitigation and safety considerations.

Flow-3D is a precise and efficient CFD solution software that has been widely used in dam break numerical simulations (Ozmen-Cagatay and Kocaman 2014), three-dimensional numerical simulations of water flow (Macián-Pérez et al. 2020), and numerical simulations of debris flows (Xu et al. 2015), flood processes (Gems et al. 2016; Zhuang et al. 2020), landslide surges (Ersoy et al. 2019), and scour evolution (Epely-Chauvin et al. 2015). Flow-3D adopts the VOF algorithm, which can completely describe the free surface and can be used for landslide movement process simulation. The simulation results of various previous studies agree well. Gabl et al. (2015) used Flow-3D to simulate the landslide sliding and surge process of reservoir landslides. The landslide model could be suitably adapted to the terrain, and the landslide sliding behavior suitably agreed with that in previous cases. Hu et al. (2019) described similar characteristics of the entrainment effect during avalanches based on simulations with this software. Hu et al. (2020) used Flow-3D to simulate the dynamic evolution process of the Baige landslide through the method of equivalent fluid method, and the simulation results show that the landslide formation is consistent with field observations. Xu et al. (2015) utilized Flow 3D to simulate the secondary debris flow disaster initiated by the volcanic eruption in the Changbai Mountain. The calculation results

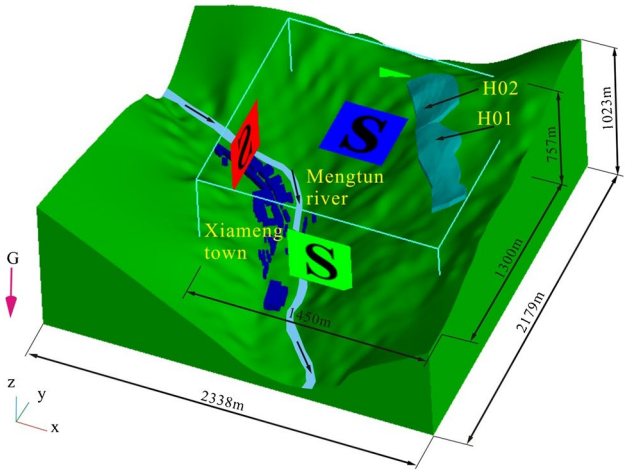

Fig. 8 Model of the landslides in Qingliu village

Table 1 Parameter description for silty clay

Parameters	Density (kg/m^3)	Viscosity (kg/m/s)	Shear modulus (Pa)	Yield stress (Pa)
Silty clay	1900	0.1	1.2×10^5	3.0×10^5

under extreme assumptions notably agreed with the distribution of debris flows during the volcanic eruption in this area. Yin et al. (2015) simplified the Qianjiangping landslide motion as a rigid body circular motion based on general moving objects (GMO) in Flow-3D and confirmed the validity of it combined with the field survey. Results show that the GMO model could reflect the movement process of the landslide.

Method

The landslides in Qingliu village are soil landslides, and there are fluid characteristics in the process of landslide movement after instability; consequently, the equivalent fluid method was used for simulation. The landslide range was determined via field investigation, and the landslide was simulated under the condition of heavy rain. Considering emergency avoidance and safety, the average thickness of the landslide is 40 m, the volume of the H01 landslide model is approximately 4.23×10^6 m^3, and the volume of the H02 landslide model is approximately 3×10^6 m^3. A landslide model was established (Fig. 8), the grid was divided, the numerical model was set, and the dynamic evolution process was simulated and analyzed.

Model description

The bulk density of the H01 and H02 slide bodies in the Qingliu village landslide in Li County is 18.5 kN/m^3 under natural conditions. Under rainstorm conditions, the slide bodies are partially saturated with water. Relevant parameter values of the slide bodies are listed in Table 1. The gravity model, viscoelastic-plastic model, viscosity model, and turbulence model were used to simulate the movement process. Among them, the gravity model is used to describe the action of gravity. The viscoelastic-plastic model is the core part in the equivalent fluid method which take the kinematic viscosity, shear modulus, yield strength, and density into consideration thus the masses are equivalent to a non-Newtonian fluid. The viscoelastic-plastic model includes the elastic stress term in the fluid stress tensor. The viscoelastic-plastic material refers to the elastic solid material under yield stress and the viscous liquid in numerical simulation. This model can be used to simulate viscoelastic fluid. Viscosity force and turbulence are calculated in the viscosity and turbulence model. The flow resistance is determined by the velocity, turbulent flow, and the surface roughness of boundary. The resistance that the equivalent fluid flow the solid boundary, besides, the resistance caused by turbulence within a fluid are calculated by this model. Experimental flow and renormalized group models were selected as viscosity and turbulence models, respectively. The mass continuity equation and mass motion model (Flow science 2016; Hu et al. 2020) can be expressed as follows:

$$\frac{\partial u}{\partial t} + \frac{1}{V_F}\left\{ uA_x\frac{\partial u}{\partial x} + vA_y\frac{\partial u}{\partial y} + wA_z\frac{\partial u}{\partial z} \right\} = -\frac{1}{\rho}\frac{\partial p}{\partial x} + G_x + f_x - b_x - \frac{R_{SOR}}{\rho V_F}\left(u - u_w - \delta u_s\right) \tag{1}$$

$$\frac{\partial v}{\partial t} + \frac{1}{V_F}\left\{ uA_x\frac{\partial u}{\partial x} + vA_y\frac{\partial u}{\partial y} + wA_z\frac{\partial v}{\partial z} \right\} = -\frac{1}{\rho}\left(R\frac{\partial p}{\partial y}\right) + G_y + f_y - b_y - \frac{R_{SOR}}{\rho V_F}\left(v - v_w - \delta v_s\right) \tag{2}$$

$$\frac{\partial w}{\partial t} + \frac{1}{V_F}\left\{ uA_x\frac{\partial w}{\partial x} + vA_y\frac{\partial w}{\partial y} + wA_z\frac{\partial w}{\partial z} \right\} = -\frac{1}{\rho}\frac{\partial p}{\partial z} + G_z + f_z - b_z - \frac{R_{SOR}}{\rho V_F}\left(w - w_w - \delta w_s\right) \tag{3}$$

where G_i is the body acceleration, f_i is the viscous acceleration, b_i denotes the flow losses in porous media or across porous baffle plates, and the final terms account for the injection of mass at source f_i represented by geometry component ($i = x, y, z$); (u, v, w) are in the coordinate directions velocity components; V_F is the fraction of the volume open to flow, ρ is the density of the sliding mass, P is the pressure of the sliding mass, R_{SOR} is a mass source, A_x, A_y, and A_z are the fractions of the area open to flow along the x, y, and z directions, respectively, (u_w, v_w, w_w) are the velocities of the source component, and (u_s, v_s, w_s, w_w) (u_s, v_s, w_s) are the velocities of the sliding mass at the surface of the source relative to the source itself.

$$\frac{\partial \varepsilon_T}{\partial t} + \frac{1}{V_F}\left\{ uA_x \frac{\partial \varepsilon_T}{\partial x} + vA_y R\frac{\partial \varepsilon_T}{\partial y} + wA_z \frac{\partial \varepsilon_T}{\partial z} \right\} = \frac{CDIS1 \cdot \varepsilon_T}{k_T}\left(P_T + CDIS3 \cdot G_T\right) + Diff_e - CDIS2\frac{\varepsilon_T^2}{k_T} \tag{4}$$

$$\frac{\partial k_T}{\partial t} + \frac{1}{V_F}\left\{ uA_x \frac{\partial k_T}{\partial x} + vA_y \frac{\partial k_T}{\partial y} + wA_z \frac{\partial k_T}{\partial z} \right\} = P_T + G_T + Diff_{k_T} - \varepsilon_T \tag{5}$$

$$Diff_e = \frac{1}{V_F}\left\{ \frac{\partial}{\partial x}\left(v_e A_x \frac{\partial \epsilon_T}{\partial x} \right) + R\frac{\partial}{\partial y}\left(v_e A_y R\frac{\partial \varepsilon_T}{\partial y} \right) + \frac{\partial}{\partial z}\left(v_e A_z \frac{\partial \varepsilon_T}{\partial z} \right) + \xi \frac{v_e A_x \varepsilon_T}{x} \right\} \tag{6}$$

$$Diff_{k_T} = \frac{1}{V_F}\left\{ \frac{\partial}{\partial x}\left(v_e A_x \frac{\partial k_T}{\partial x} \right) + R\frac{\partial}{\partial y}\left(v_e A_y R\frac{\partial k_T}{\partial y} \right) + \frac{\partial}{\partial z}\left(v_e A_z \frac{\partial k_T}{\partial z} \right) + \xi \frac{v_e A_x k_T}{x} \right\} \tag{7}$$

where k_T is the turbulent kinetic energy, P_T is the produced avalanche kinetic energy, G_T is the avalanche energy produced by buoyancy, ε_T is the rate of avalanche energy dissipation, $Diff_e$ and $Diff_{k_T}$ are the diffusion terms, which are related to V_F, A_i, and specific diffusion coefficients, $CDIS1$ and $CDIS3$ are dimensionless parameters with constant values of 1.42 and 0.2, respectively, and $CDIS2$ can be determined from k_T and P_T in the RNG$k-\varepsilon$ model.

The viscoelastic-plastic model can be used to describe the viscous stress and elastic stress of the sliding body, and the landslide is equivalent to a viscous liquid. The viscoelastic-plastic model can be defined as

$$\frac{\partial \tau_E'}{\partial t} + \nabla \cdot \left(u\tau_E'\right) = 2GD'(x,t) + \tau_E' \cdot W + W^T \cdot \tau_E' \tag{8}$$

$$\frac{\partial p}{\partial t} + \nabla \cdot (up) = -K\dot{e} + 3\alpha K\left[\frac{\partial T}{\partial t} + \nabla \cdot (uT)\right] \tag{9}$$

$$\tau_{\mathrm{E}}' = 2GE' \tag{10}$$

Where τ_E' is the deviatoric part of the elastic stress, u is the shear elastic modulus, G is the shear elastic modulus, E' is the deviatoric part of incremental strain, the D' is the deviatoric part of the strain rate tensor, W is the vorticity tensor, p is the negative mean isotropic stress, K is the bulk modulus, e is the volumetric strain, a is the linear thermal expansion coefficient, and T is the temperature.

The initial condition is zero stress at the beginning of the simulation, and the von Mises yield condition was used to predict the yield effect, which can be obtained as

$$II_{\tau_{\mathrm{E}}'} = \frac{\mathrm{Y}^2}{3} \tag{11}$$

where $II_{\tau' E}$ is the second invariant of the deviatoric part of the elastic stress tensor and Y is the yield stress limit, which can be defined by users.

$$\tau'^{*}\mathrm{E} = \sqrt{\frac{2Y^2}{3II_{\tau_{\mathrm{E}}'}}}\tau_{\mathrm{E}}' \tag{12}$$

where τ'^{*}_{E} $\tau^{'*}_{\mathrm{E}}$ is the yield-limited elastic stress tensor, which is applied to the Navier−Stokes equations to obtain the momentum balance of the fluid.

Parameter values of the landslide model

In the gravity model, the value of the gravitational acceleration is 9.81 m/s^2. viscoelastic-plastic, viscous flow, and renormalized group (RNG) models were selected, and the numerical models are explicit.

Blocks were divided by the total number of grids. The overall computation grid contained approximately 15 million grid cells, and the simulation completion time was set to 100 s. An incompressible fluid model was used for fluid calculation, and a free surface was used for liquid surface tracking.

There are several key simulation parameters in the simulation of this paper as shown in Table 1, and they are density, viscosity, shear modulus, and yield stress which are applied for the description of the equivalent fluid. The density of the equivalent is set to 1900 kg/m^3 which is equal to the sliding mass.

The shear modulus describes the material resistance to shearing. Viscoplastic materials are materials that behave as elastic solids up to their yield stress, at which time they behave as a viscous liquid. The yield stress is adopted to describe the stress limit of the fluid; if further strain were to be imposed to a point such that the elastic stress surpasses the yield stress, the material would yield and begin to flow as a liquid (Flow science 2016). The parameter viscosity is used to equivalent the influence of internal friction of the debris avalanche; higher value of viscosity means the internal friction in amplified (Hu et al. 2019).

Boundary conditions were set for the grid blocks. The bottom was defined as a wall, while the fluid near the

boundary could not move relative to the boundary, and the other boundaries were symmetric. The source area was imported by adding the fluid domain under the initial condition option, and the preset fluid was called under the fluid setting option for numerical simulation purposes.

Analysis of the landslide movement process

Flow-3D numerical simulation software was used to simulate the landslide movement process according to the parameters provided in Table 1. The kinetic evolution process was analyzed based on the simulation results. The landslide movement velocity at $t=0$, 10, 20, 30, 40, and 67 s is shown in Fig. 9, the thickness of the landslide is shown in Fig. 10, and the landslide accumulation range shown in Fig. 11 was selected to analyze the dynamic evolution process of the landslide.

As shown in Fig. 9, at $t=0$ s, the sliding mass as a whole started to move without an initial velocity, and the mass then slid downward rapidly and collected toward the gully in the sliding process. At 22 s, the landslide speeds of H01 and H02 reached maximum values of 44.8 m/s and 49 m/s, respectively. During the 22 ~ 60 s period, the speed gradually decreased, and the sliding mass stopped at 67 s.

Throughout the movement process, the sliding mass converged in the gully and was finally deposited on both sides of the Mengtun River and in residential areas of Xiameng town. The maximum deposition thickness of landslide H02 was 38.8 m in the residential areas on the right bank of the

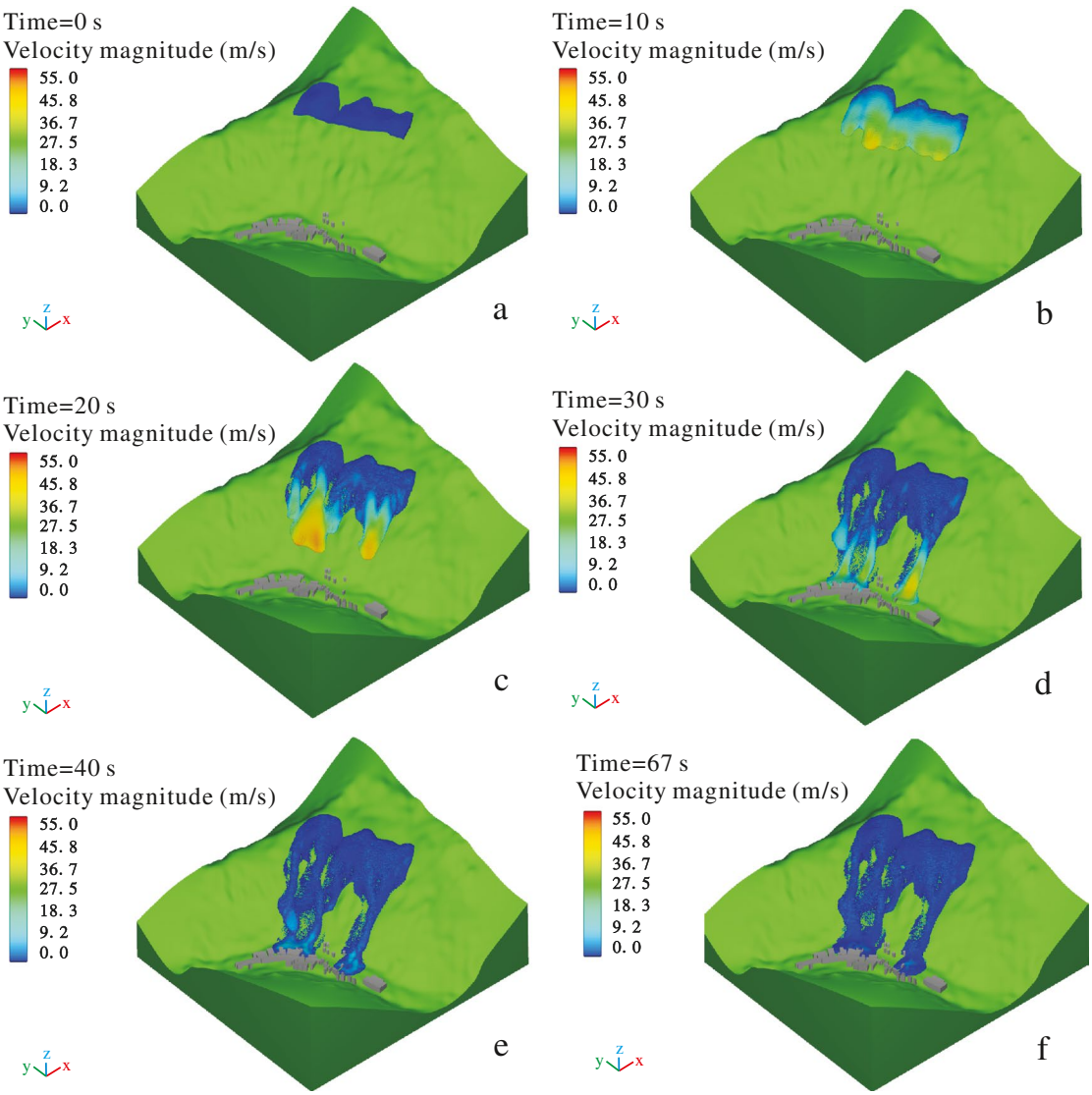

Fig. 9 Velocity magnitude of the sliding mass at the different times: **a** $t=0$ s, **b** $t=10$ s, **c** $t=20$ s, **d** $t=30$ s, **e** $t=50$ s, and **f** $t=67$ s

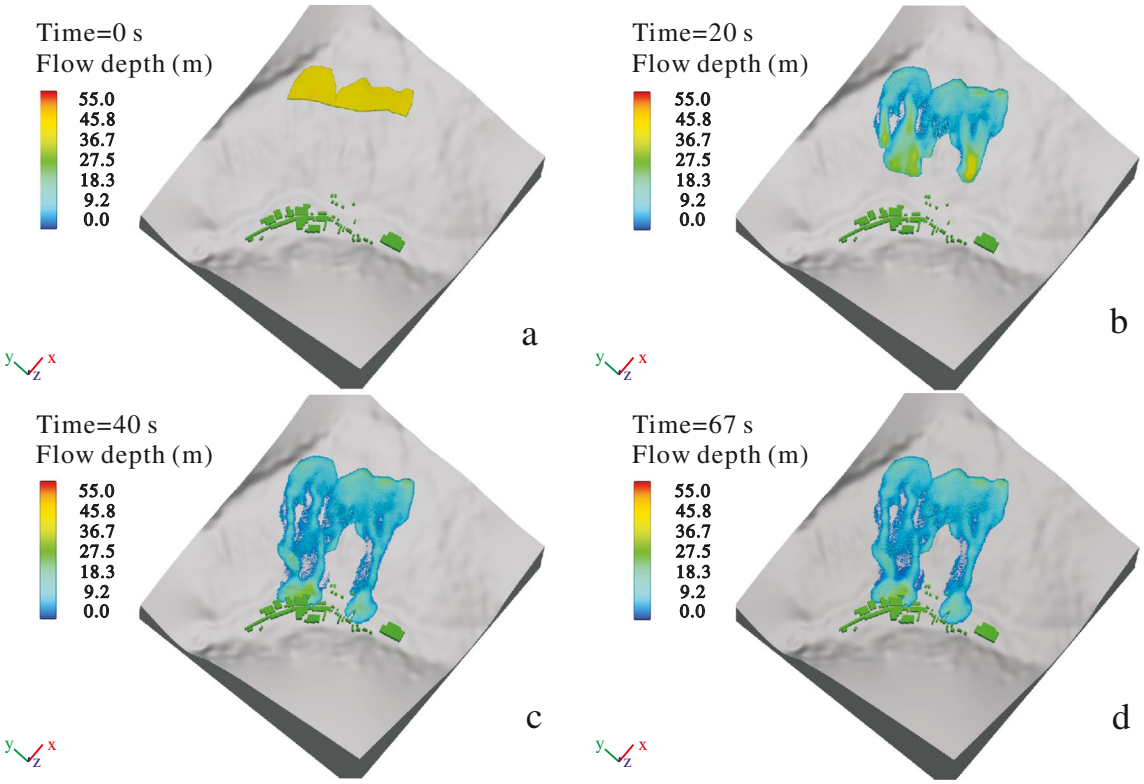

Fig. 10 Simulated deposition thickness of the sliding mass at the different times: **a** $t=0$ s, **b** $t=20$ s, **c** $t=40$ s, and **d** $t=67$ s

Mengtun River, and the maximum accumulation thickness of the H01 landslide was 24.8 m. The deposition area of the H02 landslide was approximately 360.3 m long along the river and 201 m wide across the river at the foot of the slope, while the H01 landslide was approximately 244.2 m long and 263.7 m wide across the river within the accumulation range. The simulation results clearly indicate that both landslides could cause river blocking and house burial (Fig. 11a, b), threatening the life and property safety of the residents of Xiameng town. Owing to the topography and the features of the sliding body, a sliding mass remained in the landslide source area and slope gully.

Emergency escape route in the case of landslide hazards

The landslide is located on a high and steep slope, which threatens the life and property safety of residents. Advance knowledge of the distribution of disaster points, effective monitoring of geological disaster points, release of disaster information, effective publicity, and training and emergency drills play a significant role in the success of emergency avoidance (Wei et al. 2016; Zhuang et al. 2015). Successful cases demonstrate that a disaster prevention plan is particularly important in responding to landslides (Xiao 2009). Moreover, the key to emergency avoidance lies in the geological disaster warning system and mass safeguarding system (Zhuang et al. 2015).

The town is located on the right bank of the Mengtun River, spreading in a narrow and long belt, mainly containing residential areas, primary schools, kindergartens, township government offices, and a police station. The trunk road, Xuemeng Road, passes through the town, and structures are scattered on both sides. The area threatened by landslides extends to a notable extent.

Based on the simulation results, emergency routes in response to the Qingliu village landslide were preliminarily determined, as shown in Fig. 11c. The upper road in Qingliu village is far from the landslide area, and emergency escape mainly relies on the existing village road distributed among the residential areas. In case of danger, residents should move along the village road along the direction of vertical landslide movement to the side far away from the landslide danger boundary to temporarily avoid hazardous conditions and should not use the road within the impact area of the landslide. The residents of Xiameng town can be divided into two groups according to the distribution of houses. Residents, students, and faculty near the upper reaches of Xuemeng Road should move upstream to the emergency shelter. Residents downstream should reach the emergency shelter along Xuemeng Road downstream. Moreover, to ensure an

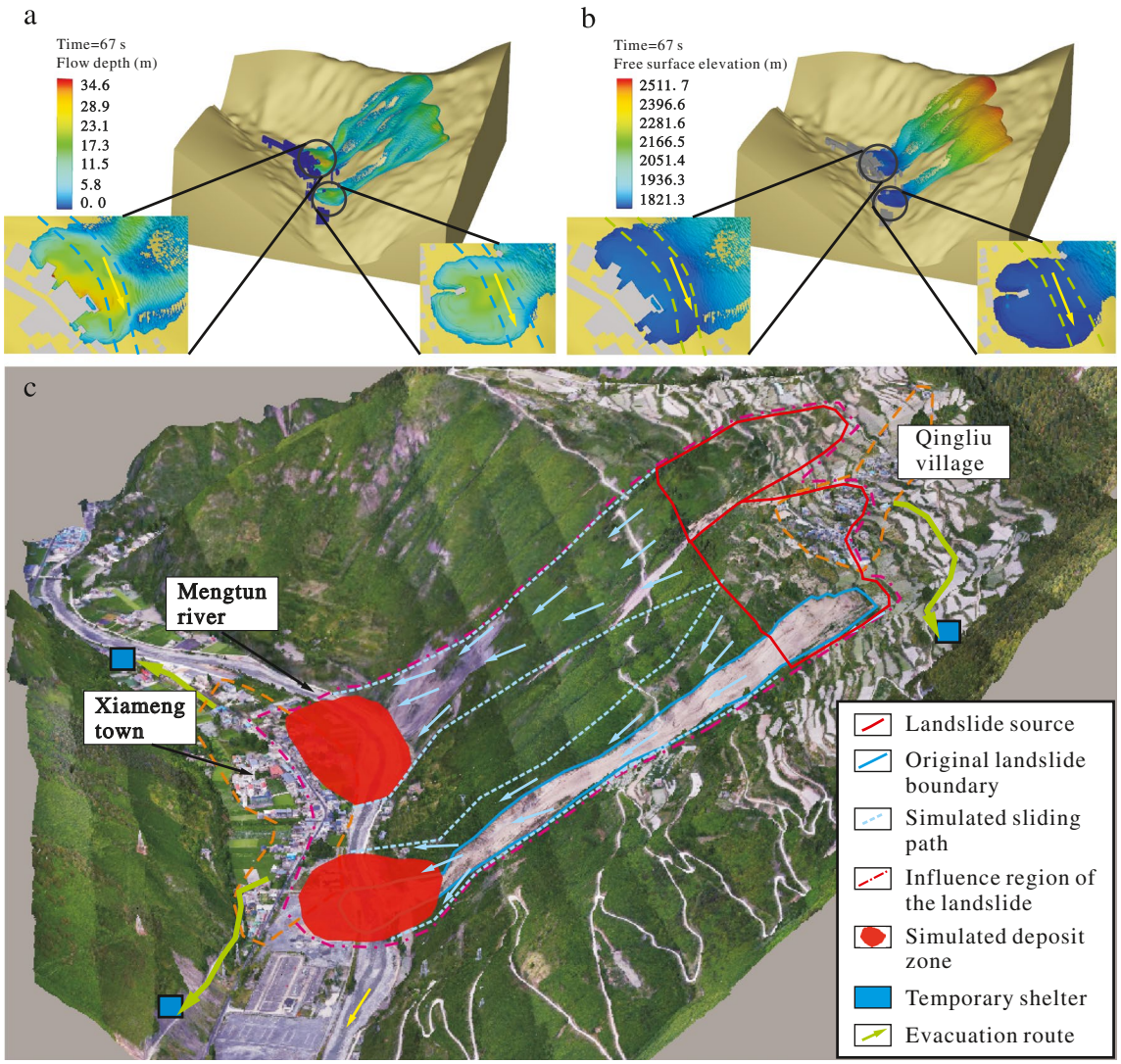

Fig. 11 Deposit and influence area of the sliding masses: **a** thickness of the deposit, **b** free surface elevation of the sliding masses, and **c** influence region of the landslides

effective emergency response, activities should be conducted in terms of disaster warning, evacuation drills, and establishing a mass safeguarding system.

Conclusions

The strong deformation zone of the H01 landslide in Qingliu village, Li County, was damaged in June and December 2020, and the strong deformation zone of the H02 landslide occurs at the continuous deformation stage. Based on field investigation and displacement monitoring, stability and other information on the overall deformation of the landform and geological conditions in the landslide area were obtained. The development characteristics and structural characteristics of landslide deformation and failure were analyzed. Along the extent of the H02 landslide, multiple extensional fractures occur, and the deformation scale is constantly expanding, which is at the creep deformation stage. The landslide traction trend is notable, and integral traction instability may occur.

Flow-3D numerical simulation software was used to simulate the landslide movement process. The most dangerous conditions were selected to simulate the sliding movement process, and the dynamic evolution process of the landslide was analyzed based on the numerical simulation results. The landslide started moving without an initial velocity, and the maximum speed of the H01 landslide reached 44.8 m/s, while the H02 landslide reached a speed of 49 m/s at 22 s. The landslide was deposited in the Mengtun River and in some of the residential areas near the river bank in Xiameng town. The maximum deposition thicknesses of H01 and H02

were 24.8 m and 38.8 m, respectively. The deposition area of the H02 landslide was approximately 360.3 m long along the river and 201 m wide across the river at the foot of the slope, while the H01 landslide was approximately 244.2 m long and 263.7 m wide across the river.

The influence region and emergency routes were initially determined according to the simulation results. The sliding masses are mainly deposited in the river and some of the residential areas on the right bank. In case of danger, the residents of Qingliu village and Xiameng town should move on the existing village road along the direction of vertical landslide movement toward the temporary shelter point far away from the landslide for protection and evacuation and avoid using the road within the danger area of the landslide.

Funding The authors gratefully acknowledge the support of the National Natural Science Foundation of China (42102316 and U20A20111) and the Open Research Fund of Key Laboratory of Reservoir and Dam Safety Ministry of Water Resources (YK323002).

Declarations

Conflict of interest The authors declare no competing interests.

References

Cui P, Chen XQ, Zhu YY, Su FH, Wei FQ, Han YS, Liu HJ, Zhuang JQ (2009) The Wenchuan Earthquake (May 12, 2008), Sichuan Province, China, and resulting geohazards. Nat Hazards 56(1):19–36

Dai FC, Xu C, Yao X, Xu L, Tu XB, Gong QM (2011) Spatial distribution of landslides triggered by the 2008 Ms 8.0 Wenchuan earthquake, China. J Asian Earth Sci 40(4):883–895

Do TN, Wu JH (2020) Simulating a mining-triggered rock avalanche using DDA: a case study in Nattai North, Australia. Eng Geol 264:105386

Epely-Chauvin G, De Cesare G, Schwindt S (2015) Numerical modelling of plunge pool scour evolution in non-cohesive sediments. Eng Appl Comput Fluid Mech 8:477–487

Ersoy H, Karahan M, Gelişli K, Akgün A, Anılan T, Sünnetci MO, Yahşi BK (2019) Modelling of the landslide-induced impulse waves in the Artvin Dam reservoir by empirical approach and 3D numerical simulation. Eng Geol 249:112–128

Fan XM, Xu Q, Scaringi G, Dai L, Li W, Dong X, Zhu X, Pei X, Dai K, Havenith HB (2017) Failure mechanism and kinematics of the deadly June 24th 2017 Xinmo landslide, Maoxian, Sichuan, China. Landslides 14:2129–2146

Fan RL, Zhang LM, Wang HJ, Fan XM (2018) Evolution of debris flow activities in Gaojiagou Ravine during 2008–2016 after the Wenchuan earthquake. Eng Geol 235:1–10

Fan XM, Scaringi G, Korup O, West AJ, Westen CJ, Tanyas H, Hovius N, Hales TC, Jibson RW, Allstadt KE, Zhang L, Evans SG, Xu C, Li G, Pei X, Xu Q, Huang R (2019) Earthquake-induced chains of geologic hazards: patterns, mechanisms, and impacts. Rev Geophys 57:421–503

Flow Science (2016) FLOW-3D V11.2 user's manual. Flow Science Inc

Gabl R, Seibl J, Gems B, Aufleger M (2015) 3-D numerical approach to simulate the overtopping volume caused by an impulse wave comparable to avalanche impact in a reservoir. Nat Hazard 15:2617–2630

Gariano SL, Guzzetti F (2016) Landslides in a changing climate. Earth Sci Rev 162:227–252

Gems B, Mazzorana B, Hofer T, Sturm M, Gabl R, Aufleger M (2016) 3-D hydrodynamic modelling of flood impacts on a building and indoor flooding processes. Nat Hazard 16:1351–1368

Hu YX, Chen ML, Zhou JW (2019) Numerical simulation of the entrainment effect during mass movement in high-speed debris avalanches. Arabian J Geosci 12:1–15

Hu YX, Yu ZY, Zhou JW (2020) Numerical simulation of landslide-generated waves during the 11 October 2018 Baige landslide at the Jinsha River. Landslides 17:2317–2328

Huang R, Pei X, Fan XM, Zhang W, Li S, Li B (2011) The characteristics and failure mechanism of the largest landslide triggered by the Wenchuan earthquake, May 12, 2008, China. Landslides 9:131–142

Kang Y, Zhao CY, Zhang Q, Lu Z, Li B (2017) Application of InSAR techniques to an analysis of the Guanling landslide. Remote Sens 9(10):1046

Li HB, Li XW, Ning Y, Jiang SF, Zhou JW (2019) Dynamical process of the Hongshiyan landslide induced by the 2014 Ludian earthquake and stability evaluation of the back scarp of the remnant slope. Bull Eng Geol Env 78(3):2081–2092

Li HB, Qi SC, Chen H, Liao HM, Cui YF, Zhou JW (2019) Mass movement and formation process analysis of the two sequential landslide dam events in Jinsha River, Southwest China. Landslides 16:2247–2258

Li HB, Xu YR, Zhou JW, Wang XK, Yamagishi H, Dou J (2020) Preliminary analyses of a catastrophic landslide occurred on July 23, 2019, in Guizhou Province, China. Landslides 17(3):719–724

Li CJ, Hu YX, Jiang N, Li HB, Zhou JW (2023) Risk assessment and landslide prevention design using numerical modeling – a case study in Qingliu, China. J Mt Sci 20(4):943–961

Liu C, Yu Z, Zhao S (2021a) A coupled SPH-DEM-FEM model for fluid-particle-structure interaction and a case study of Wenjia gully debris flow impact estimation. Landslides 18:2403–2425

Liu B, He K, Han M, Hu X, Wu T, Wu M, Ma G (2021b) Dynamic process simulation of the Xiaogangjian rockslide occurred in shattered mountain based on 3DEC and DFN. Comput Geotech 134:104122

Macián-Pérez JF, García-Bartual R, Huber B, Bayon A, Vallés-Morán FJ (2020) Analysis of the flow in a typified USBR II stilling basin through a numerical and physical modeling approach. Water 12(1):227

Ozmen-Cagatay H, Kocaman S (2014) Dam-break flow in the presence of obstacle: experiment and CFD simulation. Eng Appl Comput Fluid Mech 5:541–552

Petley D (2012) Global patterns of loss of life from landslides. Geology 40:927–930

Shan ZG, Wu H, Ni WD, Sun MJ, Wang KJ, Zhao LY, Lou YH, Liu A, Xie W, Zheng X, Guo XS (2022) Recent technological and methodological advances for the investigation of submarine landslides. J Mar Sci Eng 10(11)

Tang C, Zhu J, Li WL, Liang JT (2009) Rainfall-triggered debris flows following the Wenchuan earthquake. Bull Eng Geol Env 68:187–194

Wang D, Liu M, Zhu X, Ma H, Cheng Q, Zhu M, Chen Z, Ouyang C (2019) Failure mechanisms and deformation processes of a high-locality landslide at Tonghua Town, Li County, China, 2017. Landslides 17:165–177

Wei YJ, Chu HL, Zhuang MG, Wang CF, Bai YY (2016) Formation mechanism of Wangshan-Zhuakoushi landslide in Emei City, Sichuan Province. J Eng Geol 24:477–483

Wei J, Zhao Z, Xu C, Wen Q (2019) Numerical investigation of landslide kinetics for the recent Mabian landslide (Sichuan, China). Landslides 16:2287–2298

Wu H, Nian TK, Shan ZG, Li DY, Guo XS, Jiang XG (2023) Rapid prediction models for 3D geometry of landslide dam considering the damming process. J Mt Sci 20(4):928–942

Xiao J (2009) Theory and practice of the vital landslide hazard. Chengdu University of Technology, Chengdu, Sichuan, China

Xu PH, Yuan ZF, Li GJ, Li G, Du WH, Wang YH (2015) J Jilin Univ (Earth Sci Ed) 45:1155–1163

Yin Y, Wang F, Sun P (2009) Landslide hazards triggered by the 2008 Wenchuan earthquake, Sichuan, China. Landslides 6:139–152

Yin YP, Huang BL, Chen XT, Liu GN, Wang SC (2015) Numerical analysis on wave generated by the Qianjiangping landslide in Three Gorges Reservoir, China. Landslides 12(2):355–364

Zhang Y, Chen G, Zheng L, Li Y, Wu J (2013) Effects of near-fault seismic loadings on run-out of large-scale landslide: a case study. Eng Geol 166:216–236

Zhang LM, Zhang S, Huang RQ (2014) Multi-hazard scenarios and consequences in Beichuan, China: the first five years after the 2008 Wenchuan earthquake. Eng Geol 180:4–20

Zhou YF, Gong BW, Hu B, Xu K (2014) Evolution mode of retrogressive landslide. Chinese J Geotech Eng 36:1855–1862

Zhuang MG, Shang R, Xu WY (2015) Case analysis of geological disaster emergency hedge. Chinese J Geol Hazard Control 26:94–98

Zhuang Y, Yin Y, Xing A, Jin K (2020) Combined numerical investigation of the Yigong rock slide-debris avalanche and subsequent dam-break flood propagation in Tibet, China. Landslides 17:2217–2229

Springer Nature or its licensor (e.g. a society or other partner) holds exclusive rights to this article under a publishing agreement with the author(s) or other rightsholder(s); author self-archiving of the accepted manuscript version of this article is solely governed by the terms of such publishing agreement and applicable law.